pISSN 2384-1095
eISSN 2384-1109

iMRI 2018;22:37-49

https://doi.org/10.13104/imri.2018.22.1.37

iMRI
Investigative Magnetic Resonance Imaging

Simultaneous Unwrapping Phase and Error Recovery from Inhomogeneity (SUPER) for Quantitative Susceptibility Mapping of the Human Brain

Young-Joong Yang[1], Jong-Hyun Yoon[1], Hyun-Man Baek[2], Chang-Beom Ahn[1]

[1]Department of Electrical Engineering, Kwangwoon University, Seoul, Korea
[2]Korea Basic Science Institute, Seoul, Korea

Original Article

Received: August 22, 2017
Revised: October 19, 2017
Accepted: November 5, 2017

Correspondence to:
Chang-Beom Ahn, Ph.D.
Department of Electrical Engineering, Kwangwoon University, 20, Kwangwoon-ro, Nowon-gu, Seoul 01897, Korea.
Tel. +82-2-940-5148
Fax. +82-2-909-3159
E-mail: cbahn@kw.ac.kr

Purpose: The effect of global inhomogeneity on quantitative susceptibility mapping (QSM) was investigated. A technique referred to as Simultaneous Unwrapping Phase with Error Recovery from inhomogeneity (SUPER) is suggested as a preprocessing to QSM to remove global field inhomogeneity-induced phase by polynomial fitting.
Materials and Methods: The effect of global inhomogeneity on QSM was investigated by numerical simulations. Three types of global inhomogeneity were added to the tissue susceptibility phase, and the root mean square error (RMSE) in the susceptibility map was evaluated. *In-vivo* QSM imaging with volunteers was carried out for 3.0T and 7.0T MRI systems to demonstrate the efficacy of the proposed method.
Results: The SUPER technique removed harmonic and non-harmonic global phases. Previously only the harmonic phase was removed by the background phase removal method. The global phase contained a non-harmonic phase due to various experimental and physiological causes, which degraded a susceptibility map. The RMSE in the susceptibility map increased under the influence of global inhomogeneity; while the error was consistent, irrespective of the global inhomogeneity, if the inhomogeneity was corrected by the SUPER technique. *In-vivo* QSM imaging with volunteers at 3.0T and 7.0T MRI systems showed better definition in small vascular structures and reduced fluctuation and non-uniformity in the frontal lobes, where field inhomogeneity was more severe.
Conclusion: Correcting global inhomogeneity using the SUPER technique is an effective way to obtain an accurate susceptibility map on QSM method. Since the susceptibility variations are small quantities in the brain tissue, correction of the inhomogeneity is an essential element for obtaining an accurate QSM.

Keywords: Inhomogeneity; Magnetic susceptibility; Phase unwrapping; Quantitative susceptibility mapping

INTRODUCTION

Magnetic susceptibility is a constant that is related to the degree of magnetization of a material in response to an applied magnetic field. Tissue exposed to an external magnetic field generates its own internal magnetization or field, whose direction and

strength is given by a product of the external field strength and its susceptibility value. The internal field is a few tenths of parts per million (ppm) of the external field for most of tissues, thus it may be considered as a small perturbation field or simply a tissue-dependent magnetic field inhomogeneity. Although the susceptibility field affects the magnitude and phase of the magnetic resonance images, it is usually measured by the phase using phase sensitive magnetic resonance imaging (MRI) methods (1). Since the phase change by the susceptibility is proportional to the main magnetic field strength, it becomes an important contrast mechanism in high-field MRI (2).

The phase generated by the susceptibility is utilized to enhance image contrast in susceptibility-weighted imaging (SWI) (3). Although SWI is an effective diagnostic method for various diseases (4-8) it has a limitation due to a nonlocal character of the susceptibility field (9). To overcome the nonlocal character of the phase by the susceptibility, quantitative susceptibility mapping (QSM) to solve an inverse problem using the measured phase (10-12) was suggested. QSM has also been applied to diagnosis. For example, QSM can detect the intracranial hemorrhage, which causes an acute stroke and traumatic brain injury (13), estimate iron concentration in the brain to diagnose various neurodegenerative disorders (14), and visualize veins and venous oxygenation (15).

Besides tissue susceptibility, there are some other sources of phase in MRI, which include blood flow, chemical-dependent frequency, and main field inhomogeneity. A phased array coil also creates spatially varying phase, and eddy currents induce spatially and temporally varying phases. Phase wrapping is an obstacle to finding the true phase. Lack of the MRI signal in the background is a limiting factor to solve the QSM accurately. Thus, separation of the tissue susceptibility-induced phase from other phase sources, especially from the global field inhomogeneity-induced phase, is of prime importance in accurately solving QSM.

The global field inhomogeneity-induced phase refers to the phase in a large scale over an entire object. For instance, the phase by main magnetic field inhomogeneity related to the magnet design and construction and susceptibility-induced field from ferromagnetic or paramagnetic objects in the vicinity of the magnet including iron pieces placed near the magnet for passive shimming (16). Chemical shift, eddy currents, and physiology-related field fluctuations (17, 18) are other sources of global phase. In this paper we model the global phase by a polynomial.

Although the origins and underlying physical principles may be different for these global phases, they affect tissue susceptibility map if they are not properly removed. In QSM imaging, removal of the phase has focused on the background susceptibility-induced phase using harmonic property (12, 19, 20). However, the global phases due to chemical shift, eddy current, and physiology-related field fluctuations would not be a harmonic function, and so are not removed by the background phase removal method. The remaining phase would generate error in the susceptibility map. The tissue susceptibility field is < 0.2 ppm of the main field strength in the brain tissue (11, 21), and so can be easily overwhelmed by the global field inhomogeneity.

Although the global field inhomogeneity is a well-known problem in MRI (22-24), there have been few studies that investigate the global field inhomogeneity in conjunction with QSM.

In this paper, we propose a technique called Simultaneous Unwrapping Phase and Error Recovery from inhomogeneity (SUPER) for QSM as a means to unwrap the phase and remove the global field inhomogeneity-induced phase simultaneously, whether it is harmonic or not. The effect of the global field inhomogeneity on QSM is investigated using numerical simulations. Some experimental results obtained for 3.0T and 7.0T MRI systems are shown to demonstrate the efficacy of the proposed method.

Quantitative susceptibility map may be useful to evaluate iron-deposition in the brain tissue, which has a great potential in the diagnoses of early-stage degenerative brain diseases.

MATERIALS AND METHODS

QSM Data Acquisition

The perturbed field due to the susceptibility is measured by a gradient echo sequence with double echo acquisition. Let $I_1(x,y,z)$ and $I_2(x,y,z)$ be the reconstructed images from the echoes obtained with the echo times of TE_1 and TE_2, respectively. By the complex multiplication of the two images, with one of them complex conjugated, the phase is given by

$$\begin{aligned} p(x,y,z) &= angle\{I_2(x,y,z)\cdot I_1^*(x,y,z)\} \\ &= \gamma[\delta(x,y,z)+\sigma(x,y,z)]\Delta T \\ &= \theta(x,y,z)+\varphi(x,y,z) \end{aligned} \quad [1]$$

where γ is the gyromagnetic ratio, $\delta(x,y,z)$ is the global field inhomogeneity, $\sigma(x,y,z)$ is the perturbed field due to the susceptibility, ΔT is the difference of the echo times, TE_2 - TE_1. The phases due to the global field inhomogeneity and the susceptibility are represented by $\theta(x,y,z)$ and, $\varphi(x,y,z)$ respectively. By the complex multiplication, coil-dependent phase and other offset phase are removed. Then the reconstructed image from each receiver channel can be added together for further processing (channel summation).

QSM Processing

The phase generated by the tissue susceptibility distribution, $X(k)$ is expressed by (12)

$$\varphi(k) = (2\pi f_0 \Delta T)\, X(k) \cdot D(k) \quad [2]$$

where $\varphi(k)$ is the three-dimensional (3-D) Fourier transform of the tissue susceptibility-induced phase in Eq. [1], f_0 is the precession frequency of the main magnetic field. The dipole kernel, $D(k)$ is given by (25)

$$D(k) = \begin{cases} \frac{1}{3} - \frac{k_z^2}{k^2}, & for\ \ k \neq 0 \\ 0, & for\ \ k = 0 \end{cases} \quad [3]$$

with $k^2 = k_x^2 + k_y^2 + k_z^2$.

The measured phase may be wrapped on the interval $-\pi$ to π radians. If the phase is wrapped, then phase unwrapping is necessary. Various methods have been proposed to unwrap the phase (26-28), among which the Laplacian phase unwrapping method (26) is widely used for its simplicity and robustness to noise.

Note that susceptibilities outside the object have nonzero values. For example, the susceptibility of air is about 0.36 ppm, which is significantly different from the -9 ppm of water (tissue), thus they generate a background phase. Since no MRI signal is available in the background, removal of the background phase from the measured phase of MRI scans is necessary to obtain only the phase due to tissue susceptibilities (12, 19, 20). Among the background phase removal methods, SHARP utilizes harmonic function property of the field that satisfies the Laplace equation (12). Performance evaluation for various background phase removal methods is found in the recently published review articles (25, 29). Once the background phase is removed, the susceptibility map is given by dividing the phase by the dipole kernel in k-space as

$$X(k) = \frac{1}{2\pi f_0 \Delta T} \cdot \frac{\varphi(k)}{D(k)} \quad [4]$$

Since the dipole kernel in the k-space has zero values on the surface of corns with azimuthal angles of $\pm$ 0.96 radians from z axis, this is an ill-posed problem (11). The problem may be solved by using regularization with a priori assumption.

SUPER

SUPER is proposed to unwrap the phase and to remove the global inhomogeneity-induced phase simultaneously by a polynomial fitting, thereby reducing error in the susceptibility map. The phase due to the global inhomogeneity in Eq. [1] is first modeled by a polynomial given by

$$\theta(x,y,z) = \sum_u \sum_v \sum_w \alpha_{uvw}\, x^u y^v z^w \quad [5]$$

where α_{uvw} is the coefficient of the polynomial. The model was motivated from shim fields implemented by shim coils and shim currents (16). Shim fields consist of linear, second order, and some third order terms. Thus the polynomial model is considered as a generalization of the shim fields. In finding the model coefficients, partial derivatives of the model formula Eq. [5] is used with the phase difference data along the x, y, and z directions, which is equivalent to the partial derivatives in discrete formula with a unit voxel distance (24).

$$\begin{aligned} \frac{\partial\theta(x,y,z)}{\partial x} &= \sum_u \sum_v \sum_w u \cdot \alpha_{uvw}\, x^{u-1} y^v z^w = d^x p(x,y,z) \\ \frac{\partial\theta(x,y,z)}{\partial y} &= \sum_u \sum_v \sum_w v \cdot \alpha_{uvw}\, x^u y^{v-1} z^w = d^y p(x,y,z) \\ \frac{\partial\theta(x,y,z)}{\partial z} &= \sum_u \sum_v \sum_w w \cdot \alpha_{uvw}\, x^u y^v z^{w-1} = d^z p(x,y,z) \end{aligned} \quad [6]$$

where $d^x p(x,y,z)$, $d^y p(x,y,z)$, $d^z p(x,y,z)$ are the phase differences along the x, y, and z directions, respectively. The phase difference between adjacent voxels is usually very small, even under the global field inhomogeneity and susceptibility field; therefore the phase wrapping problem would not need to be considered with the phase difference data in Eq. [6]. Furthermore, the chemical composition dependent phase shifts are also removed in the phase difference data except at the boundaries of different chemical compositions. Since the phase difference data

at the boundaries are usually large, they can easily be identified and are excluded in applying Eq. [6]. For example, Eq. [7] defines a set of such data points where the sum of magnitudes of the phase slopes is larger than a threshold.

$$R_c\{(x,y,z)\,|\,(|d^x p(x,y,z)|+|d^y p(x,y,z)|+|d^z p(x,y,z)|)>Th)\} \quad [7]$$

where *Th* is a threshold value. Since the phase difference crossing different chemical compositions (= π for water/fat imaging for instance) is much larger than that between the same compositions, the threshold can be chosen as $\pi/2$, independent of noise.

As the perturbed field due to the susceptibility is relatively small (< 0.2 ppm in the brain tissue), and is confined to a small region, it has little effect on the model coefficients of the global inhomogeneity, and vice versa. In ultrahigh field MRI, however, large field perturbation may occur near the sinus cavity and auditory canal, due to large susceptibility differences between air and tissue. If the affected regions are relatively wide, the phase data in these regions need be excluded from the estimation of the global field inhomogeneity. Such regions can be identified using the phase difference data and a threshold similar to Eq. [7]. Magnitude data may also be used to identify such regions, where intensity is below a threshold.

Eq. [6] may be rewritten in a matrix form as

$$\begin{bmatrix} d^x p(x,y,z) \\ \vdots \\ d^y p(x,y,z) \\ \vdots \\ d^z p(x,y,z) \\ \vdots \end{bmatrix} = \begin{bmatrix} u\cdot x^{u-1}y^v z^w \\ \vdots \\ v\cdot x^u y^{v-1} z^w \\ \vdots \\ w\cdot x^u y^v z^{w-1} \\ \vdots \end{bmatrix} [\alpha_{uvw}]$$

or [8]

$$dP = M\cdot\alpha.$$

In Eq. [8] *dP* is a column vector of size (L × 1), *M* a matrix of size (L × Q), and *a* a column vector of size (Q × 1), where L is the number of data, and Q is the number of terms of the polynomial. Then the model coefficients are obtained using the least square error estimation given by (22)

$$\alpha = M^- \cdot dP$$

with [9]

$$M^- = (M^T \cdot M)^{-1} \cdot M^T.$$

Since the number of phase difference data (L) is several orders of magnitude larger than that of the model coefficients (Q) to be estimated, the equation is heavily over-determined. Thus, the model coefficients can be obtained very stably and robust to noise in spite of the noise amplification, by taking the differences of the phases. If the model coefficients are determined, the estimated global inhomogeneity phase is subtracted from the measured phase. Thus the remaining phase is only the tissue susceptibility phase, which is small enough in the brain not to generate phase wrapping.

RESULTS

Simulation

For numerical simulation, three-dimensional (3D) head-mimicked tissue susceptibility data (phantom) were used (30). The matrix size of the phantom was 256 × 256 × 91 with voxel resolution of 0.94 mm × 0.94 mm × 1.5 mm. The susceptibility values were from -0.44 to 0.21 ppm (mostly -0.06 – 0.09 ppm). The data represent relative susceptibility values with respect to a reference material (e.g., cerebrospinal fluid). The relative susceptibility values had little effect in testing the global inhomogeneity effect on QSM. The susceptibility values outside the brain were set to zero. Field perturbations at the tissue-air interfaces were excluded in the simulation. The main field strength was assumed as 3.0T, with the echo time of 8.1 ms for generation of the susceptibility field-induced phase.

To investigate effect of the global field inhomogeneity on QSM, three types of inhomogeneity were considered. One was arbitrarily generated using a polynomial of degree 4 (type-1), and the two others were based on the measured inhomogeneity from a 3.0T (type-2) and 7.0T (type-3) MRI systems. The type-2 and 3 inhomogeneity was measured experimentally using a uniform water phantom. Sequence and experimental parameters were similar to those used for *in-vivo* experiments given in the following section. The measured inhomogeneity was modeled with polynomials of degree 8. The degree of the polynomial was chosen experimentally for a minimum variance of the remaining phase after the inhomogeneity correction with the polynomial model for a uniform phantom. Generally the variance decreases as the degree of polynomial increases; however it showed saturation for degrees above 6. All three

types of inhomogeneity did not satisfy the Laplace equation.

The global inhomogeneity phase was added to the tissue susceptibility phase. Since the susceptibility-induced phase ranged -0.6 - 0.4 radians, while the inhomogeneity induced phase ranged -5.8 - 9.2 radians, the combined phase was dominated by the global inhomogeneity. The wrapped phase was used as the input to the simulation.

Figure 1 depicts an axial plane of the susceptibility map (a) and corresponding tissue phase (b) generated by Eq. [2]. The combined wrapped phase with the global inhomogeneity of type-1 (c), remaining phase after SUPER (d), and the difference (e) are shown. The susceptibility map is in ppm, and all the phases are in radians. Note that the scale in (e) is 10 times smaller compared to those in (b) and (d).

Simulation was performed with and without the global inhomogeneity correction, and root mean square error (RMSE) in the susceptibility map was evaluated. The processing flow without correction consisted of 1) Laplacian phase unwrapping (26), 2) removal of the background susceptibility-induced phase by SHARP (12), and 3) solving the susceptibility map from the tissue phase. The processing path with the correction consisted of 1) global inhomogeneity correction by SUPER, 2) removal of the background phase by SHARP, and 3) solving the susceptibility map. Note that only the first step is different in the comparison. We used identical codes for SHARP and solving the susceptibility map for both processing.

For SHARP, the size of filter kernel was 7 × 7 × 7 voxels (radius of about 3.3 mm), and truncation level was set as 0.05. A regularization method that minimizes the L1 norm of total generalized variation (TGV) was used in solving the susceptibility map (31, 32). Regularization parameters for TGV were set identical as was done previously (30).

Under the global inhomogeneity of type-1, sampled results without (upper row) and with (lower row) the correction of global inhomogeneity phase are shown in

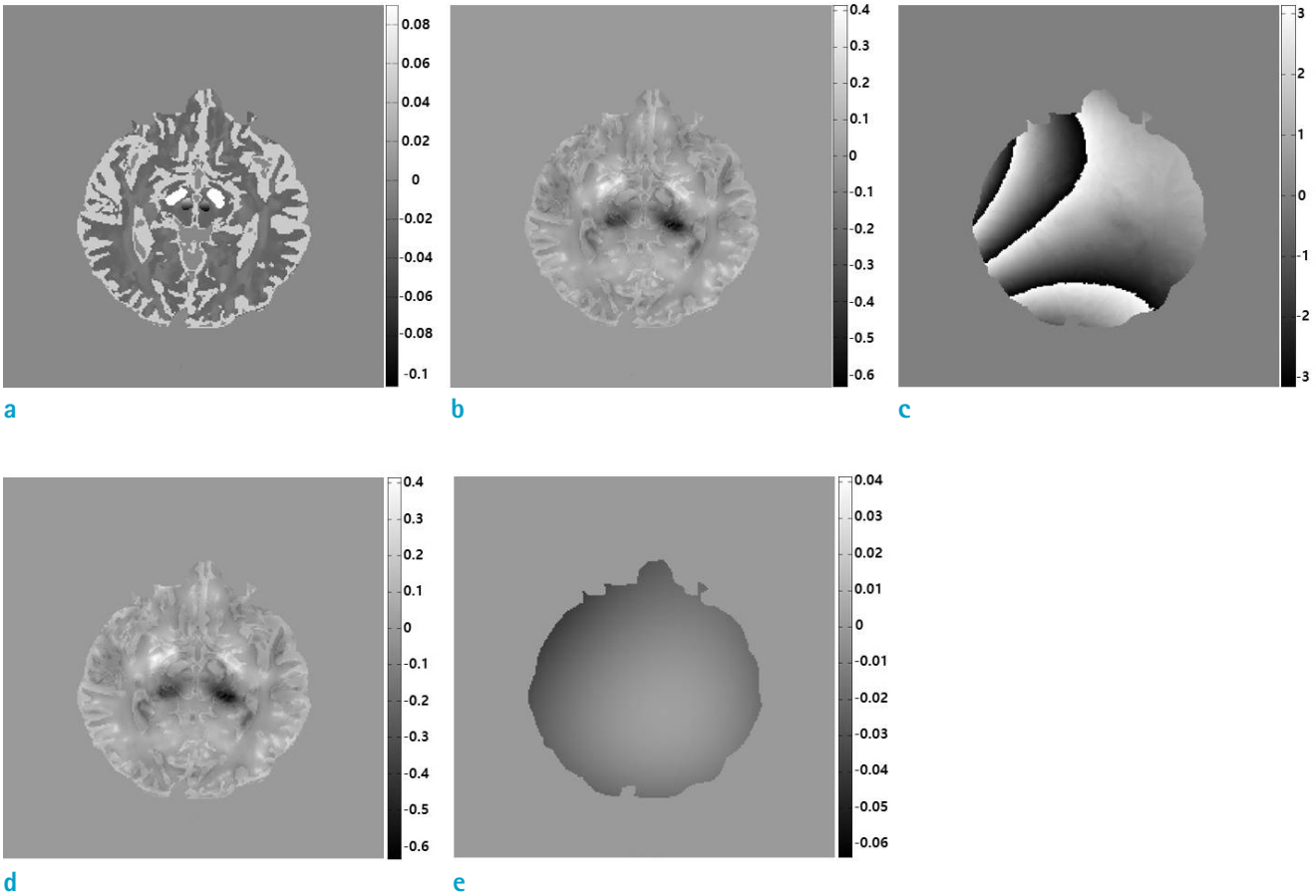

Fig. 1. Numerical phantom for the simulation: (a) An axial plane of the susceptibility data, (b) corresponding tissue phase, (c) combined phase with the global inhomogeneity-induced phase, (d) remaining phase after the global phase removal by SUPER, and (e) the difference between (b) and (d).

Figure 2: (a) unwrapped phase by the Laplacian unwrapping (b) phase after SHARP and (c) susceptibility map; and (d) unwrapped phase by SUPER, (e) phase after SHARP, and (f) susceptibility map. The global inhomogeneity-induced phase still remained in the unwrapped phase (a), whereas the phase was removed in (d). A large portion of the global inhomogeneity phase was removed by SHARP (b), while the global phase was already removed by SUPER, the contribution by SHARP was limited in (e).

The errors of the susceptibility maps are shown in Figure 3. They comprised (a) true susceptibility map, (b) error without global inhomogeneity correction, (c) error with global inhomogeneity correction, and (d) susceptibility map obtained from the global inhomogeneity-induced phase. Larger error was found in the susceptibility map without global inhomogeneity correction (b), compared to that with the correction (c). The error in the susceptibility map (b) was similar to that from the global inhomogeneity-induced phase (d), ensuring the error was due to the global inhomogeneity.

The susceptibility maps under the three types of inhomogeneity are shown in Figure 4 with the global inhomogeneity phases for coronal planes: (a) global inhomogeneity, (b) true susceptibility maps, (c) susceptibility maps obtained without global inhomogeneity correction, (d) susceptibility maps with the global inhomogeneity correction by SUPER. The maps at the top row were under the inhomogeneity modeled from a 3.0T MRI, the middle row under the inhomogeneity from a 7.0T MRI, and the bottom row under the inhomogeneity without a physical model. As seen in this simulation, larger errors were found in the susceptibility maps without global inhomogeneity correction (c) compared to those with the correction (d).

Table 1 summarizes RMSE in the susceptibility map

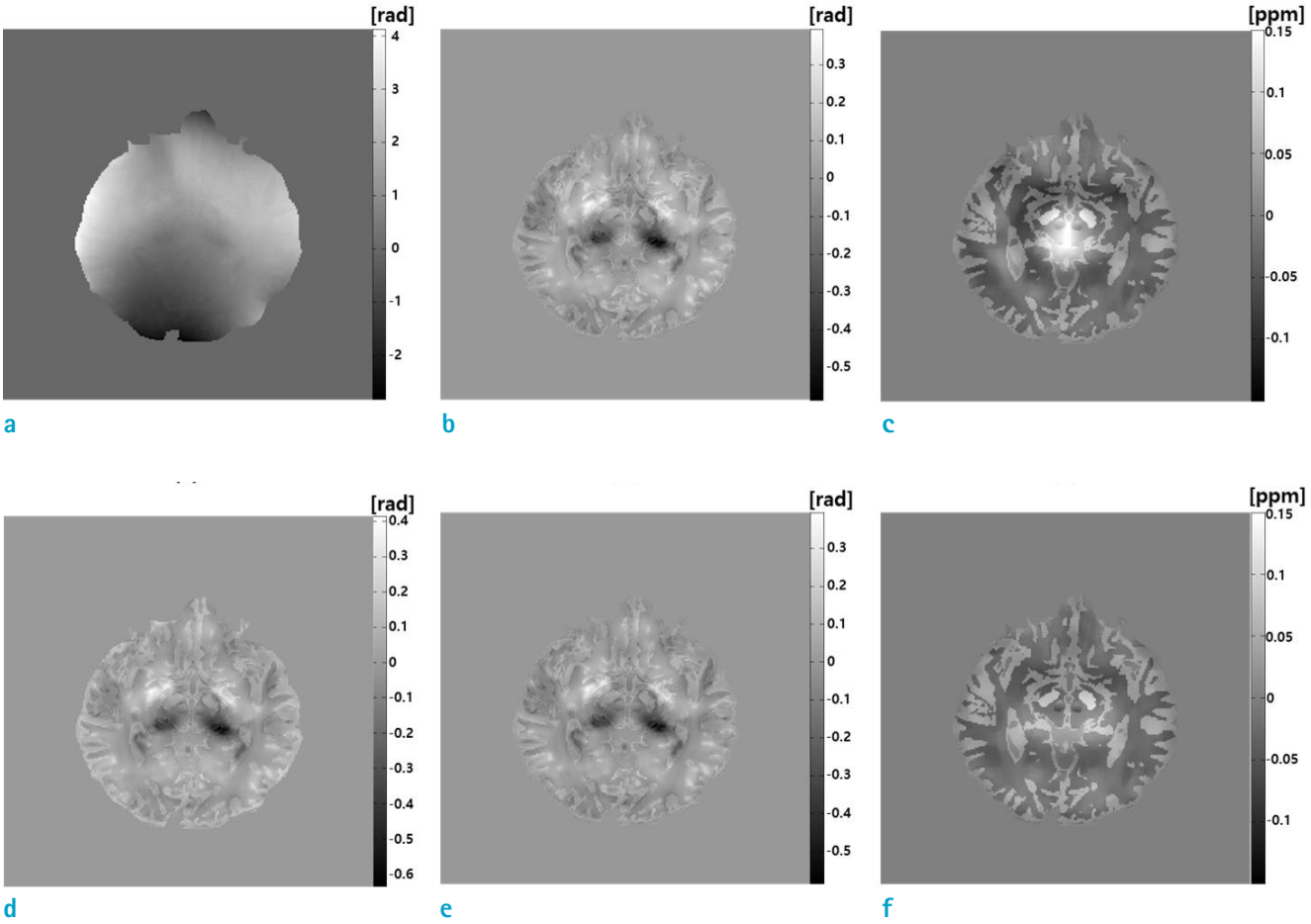

Fig. 2. The QSM without, and with the global inhomogeneity correction are shown in the upper and lower rows, respectively: (a) unwrapped phase by the Laplacian unwrapping, (b) phase after removal of the background susceptibility-induced phase by SHARP, and (c) susceptibility map; and (d) phase after SUPER, (e) phase after SHARP, and (f) susceptibility map.

over the entire object without, and with, the global inhomogeneity correction. The RMSE for the input of unwrapped phase are also shown in the parenthesis.

The RMSE without global inhomogeneity was shown in the first column. The nonzero RMSE was partially due to the error in the tissue susceptibility phase inside the object caused by the background phase removal method (SHARP). The RMSE was also attributed to the tissue phase not available outside the object. Note that correcting the global inhomogeneity did not increase RMSE, even under non-global inhomogeneity.

From the second to fourth columns, the RMSEs increased under global inhomogeneity, as shown in the upper row when global inhomogeneity correction was not applied, while the RMSEs were consistent, as shown in the lower row with the inhomogeneity correction. The RMSEs for wrapped and unwrapped phases appeared almost the same throughout the simulation. Thus, phase unwrapping is not a

Table 1. RMSE of Susceptibility Map in PPM without and with Global Inhomogeneity Correction, RMSE for Unwrapped Phase in Parenthesis

QSM method	Global inhomogeneity			
	None	Non-physical model	Modeled from a 3T MRI	Modeled from a 7T MRI
QSM without global inhomogeneity correction	0.0096 (0.0096)	0.0168 (0.0168)	0.0191 (0.0191)	0.0160 (0.0160)
QSM with global inhomogeneity correction (SUPER)	0.0096 (0.0096)	0.0096 (0.0096)	0.0102 (0.0101)	0.0102 (0.0101)

MRI = magnetic resonance imaging; PPM = parts per million; QSM = quantitative susceptibility mapping; RMSE = root mean square error; SUPER = simultaneous unwrapping phase and error recovery from inhomogeneity

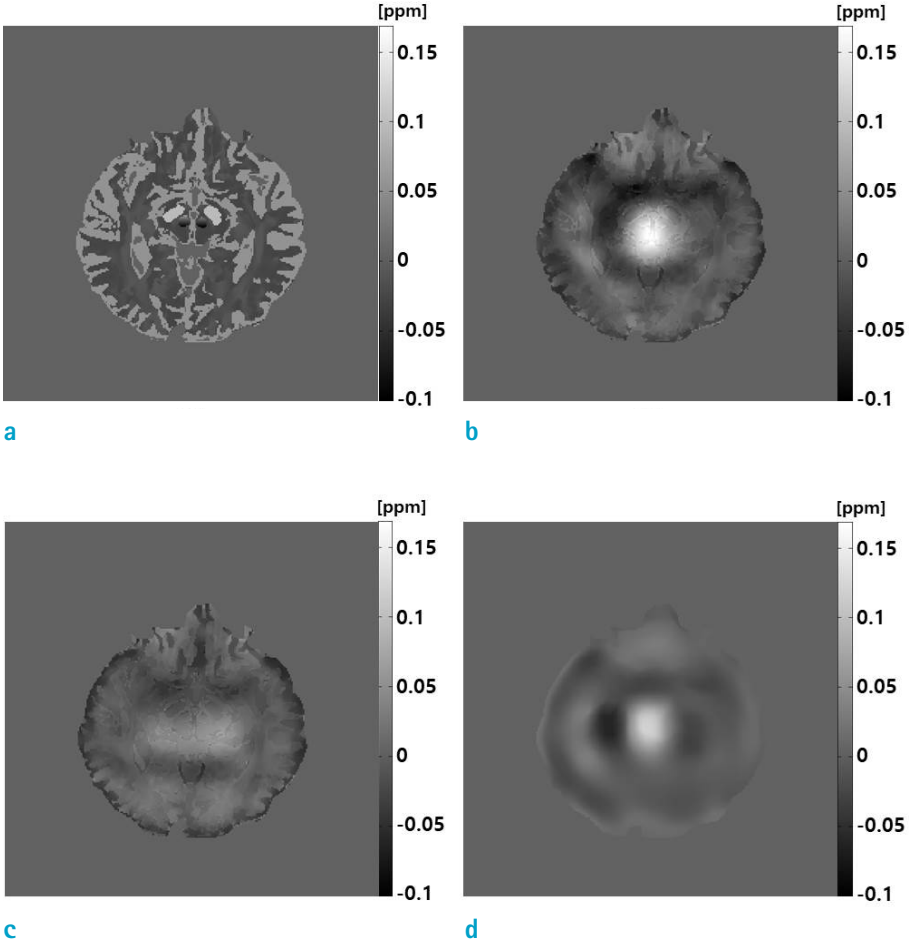

Fig. 3. Errors of the susceptibility map are shown: (a) True susceptibility map, (b) error of the map without global inhomogeneity correction, (c) error of the map with the global inhomogeneity correction, and (d) susceptibility map from the global inhomogeneity-induced phase. Note the similarity between (b) and (d), which ensures that the error is due to the global inhomogeneity.

major source of error for the susceptibility map for both the Laplacian phase unwrapping and SUPER.

In Vivo Experiments

In vivo head QSM imaging was performed using Philips 3.0T (Achieva 3.0T TX, Philips Medical System, the Netherlands) and 7.0T (Achieva 7T, Philips Medical Systems, the Netherlands) MRI systems at the Korea Basic Science Institute. A 32-channel head array coil and a dual-echo 3D fast field echo (FFE) sequence were used in 3.0T experiments. The scan parameters were: TR = 30 ms, TE1 = 8.1 ms, TE2 = 20.3 ms, RF flip angle = 10°, voxel size = 0.5 mm × 0.5 mm × 1.0 mm, BW = ± 19.04 kHz, scan time = 8.96 min. For 7.0T *in-vivo* experiments, a 32-channel head array coil and a dual-echo 3D FFE sequence were used. The scan parameters were: TR = 30 ms, TE1 = 7.0 ms, TE2 = 17.88 ms, RF flip angle = 15°, voxel size = 0.5 mm × 0.5 mm × 1.0 mm, BW = ± 21.50 kHz, scan time = 8.96 min. The matrix size was 448 × 448 × 40 for both *in vivo* data. Compressed sensing and parallel imaging were not employed.

After acquisition, the channel summation was conducted. For comparison QSM processing was carried out in two ways. One was conventional QSM processing without correction of the global inhomogeneity phase, which consisted of 1) Laplacian phase unwrapping, 2) removal of the background phase by SHARP, and 3) solving the susceptibility map from the tissue phase. The other was with the correction of the global inhomogeneity phase, which consisted of 1) global inhomogeneity correction by SUPER, 2) SHARP, and 3) solving the susceptibility map.

As to the processing parameters, size of the filter kernel was 9 × 9 × 9 voxels (radius of about 2.3 mm) for SHARP following Bilgic et al. (32). Other parameters for SHARP and TGV were set identical as in the simulation.

Figure 5 shows sample results of QSM imaging (axial, sagittal, and coronal views from top to bottom) at 3.0T MRI system. The top row presents magnitudes (a), measured phases (b), and the estimated inhomogeneity (c). The middle row shows the tissue susceptibility-induced phases without (d), and with (e), the global inhomogeneity correction, and the difference (f). The bottom row shows the susceptibility maps without (g), and with (h), the global inhomogeneity

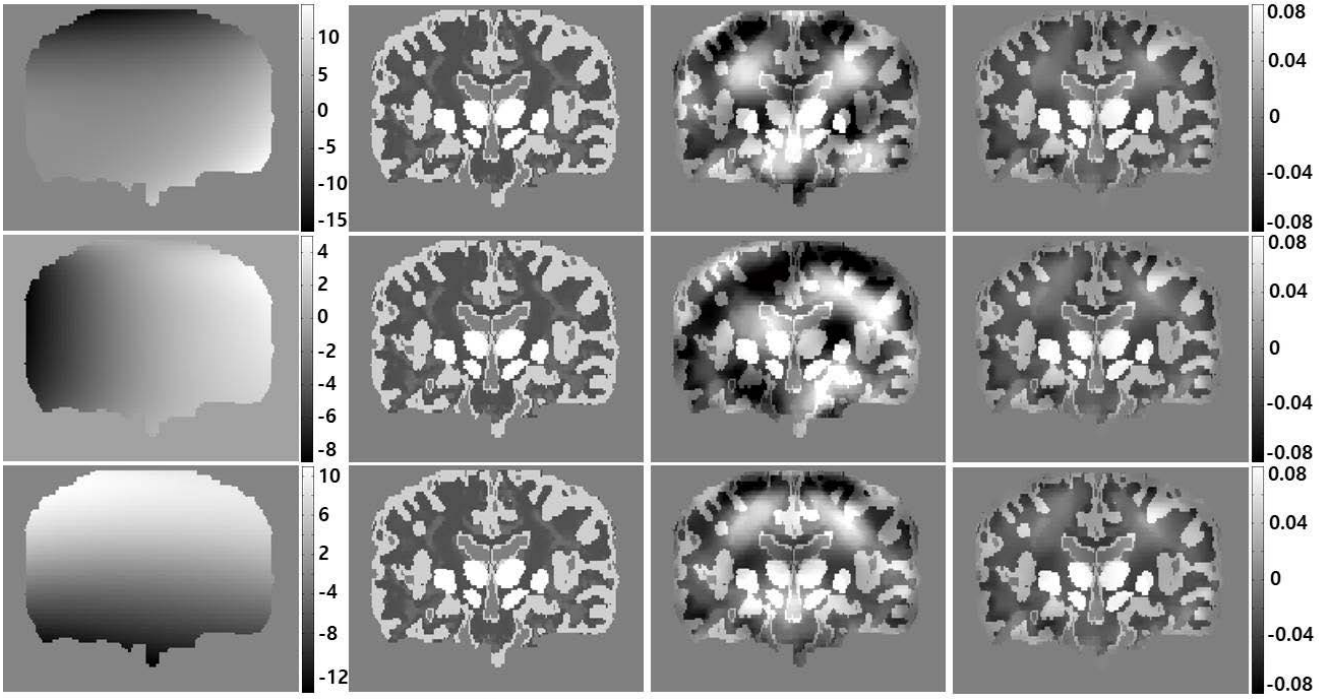

Fig. 4. Susceptibility maps are shown under the three inhomogeneity types: (a) global inhomogeneity phase, (b) true susceptibility maps, (c) susceptibility maps obtained without global inhomogeneity correction, and (d) susceptibility maps obtained with the global inhomogeneity correction by SUPER. The global inhomogeneity is modeled from a 3.0T MRI, a 7.0T MRI, and a non-physical model, from top to bottom.

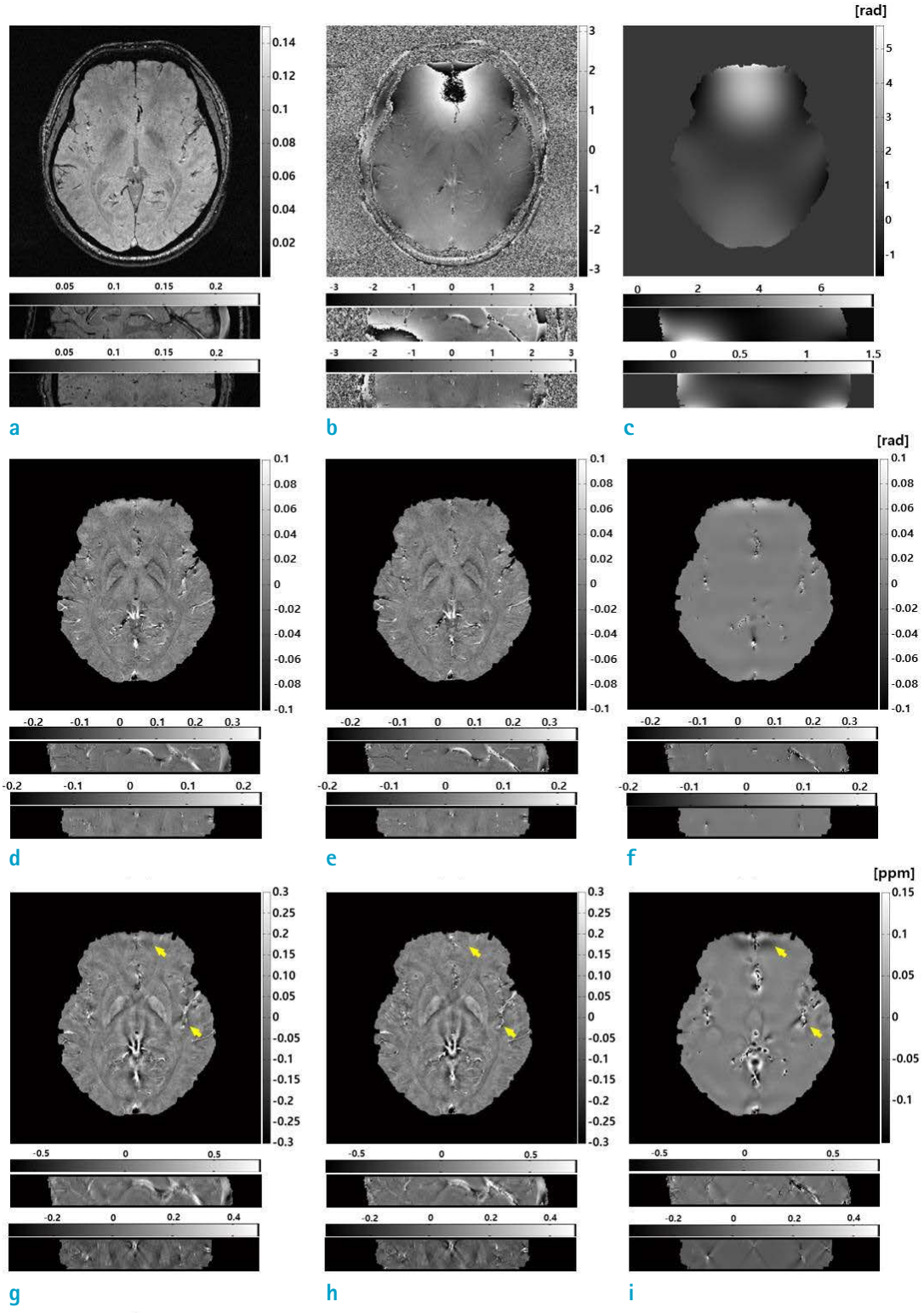

Fig. 5. *In vivo* QSM imaging at 3.0T MRI. Axial, sagittal, and coronal planes are shown from top to bottom: (a) Magnitude images, (b) wrapped phase images, (c) estimated global inhomogeneity by SUPER, (d) and (e) tissue susceptibility-induced phases without and with the global inhomogeneity correction, respectively, (f) difference, (g) and (h) susceptibility maps without and with the global inhomogeneity correction, respectively, and (i) difference. Distinctly different regions in the susceptibility maps are marked with small arrows.

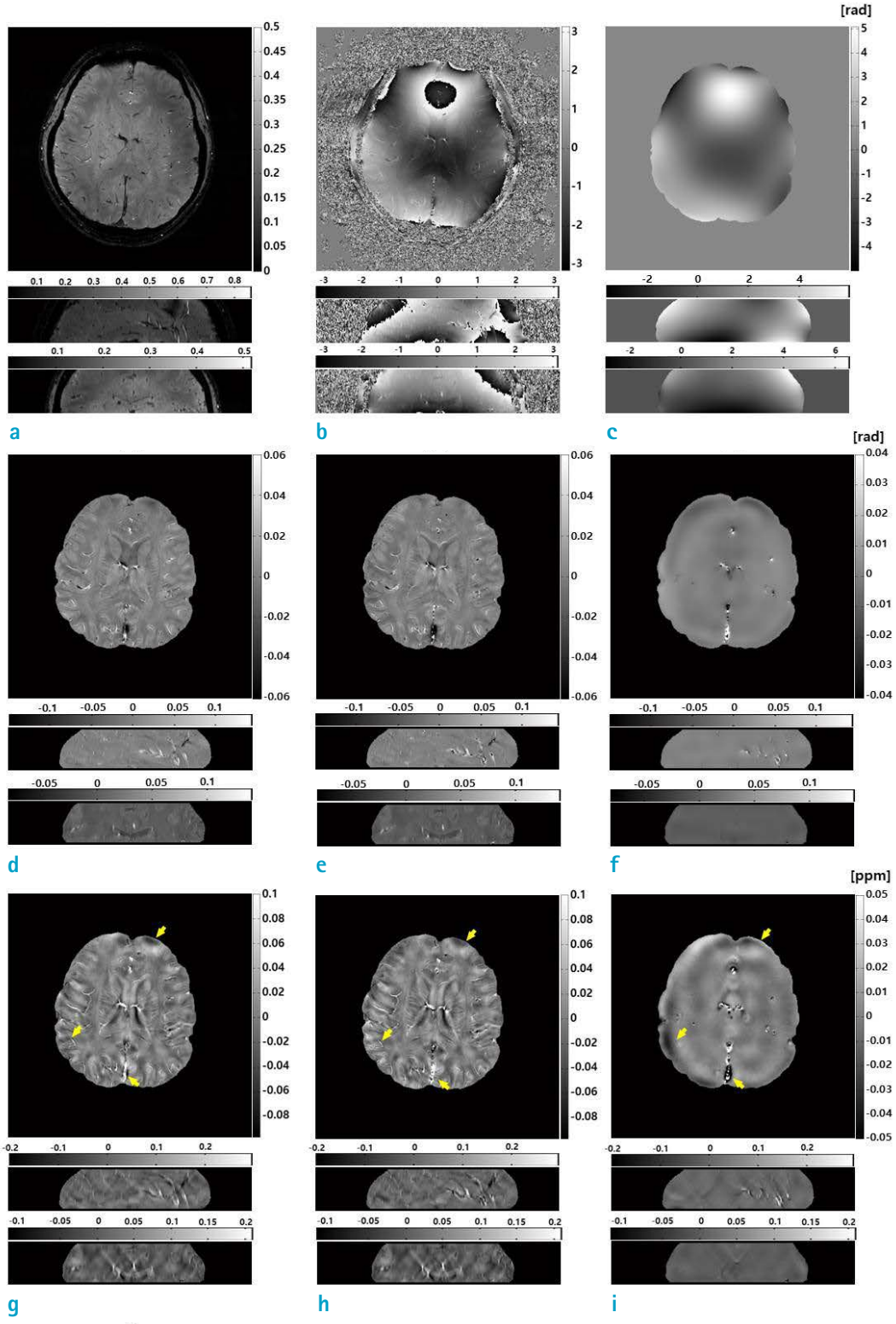

Fig. 6. *In vivo* QSM imaging for 7.0T MRI. Axial, sagittal, and coronal planes are shown from top to bottom: (a) magnitudes, (b) wrapped phases, (c) estimated inhomogeneity by SUPER, (d) and (g) tissue susceptibility-induced phase and the susceptibility map without global inhomogeneity correction, (e) and (h) tissue phase and susceptibility map with the global inhomogeneity correction, and (f) and (i) differences between the two phases and the susceptibility maps, respectively. Regions of distinct differences in the susceptibility maps are marked with small arrows.

correction, and the difference (i).

The magnitude images (a) are in an arbitrary scale, the measured phases (b), the estimated inhomogeneity (c), and the tissue susceptibility related phases (d-f) are presented in radians, and the susceptibility maps (g-i) are presented in ppm. Regions of distinct differences are marked with small arrows. The global inhomogeneity phase was removed by SUPER with a polynomial of degree 9. Although the coefficients corresponding to non-existent inhomogeneity terms would appear small, modeling of the polynomial with a large degree is not recommended due to a potential over fitting problem. Low frequency variations were found in the differences (f, i) which corresponded to the global inhomogeneity (c). For example large differences were found in the frontal lobes marked by a small arrow (i), which corresponded to the large inhomogeneity (c). Some errors in small vascular structures were seen at the middle right without global inhomogeneity correction (g), which disappeared with the correction (h).

In vivo head QSM imaging of a volunteer using the 7.0T MRI system is shown in Figure 6. Magnitude and phase images are shown in (a) and (b), estimated inhomogeneity in (c), tissue susceptibility-induced phase without (d), and with (e), the global inhomogeneity correction, and the difference (f). The susceptibility maps without (g), and with (h), the global inhomogeneity correction, and the difference (i) are shown.

Some regions of distinct differences are marked with small arrows. The global phase was estimated by SUPER with a polynomial of degree 9. As seen in Figure 6, better resolution was obtained with the global inhomogeneity correction. For example, small vascular structures were more clearly seen at the middle left of the map (h). Low frequency ripples in frontal lobes were also reduced in (h) compared to (g). Since the susceptibility values varied by small quantities (a few 0.01 ppm), they were sensitive to small variations, such as small ripples and blurring due to the global inhomogeneity.

DISCUSSION

We propose a method to remove a global field inhomogeneity-induced phase by approximating it with a polynomial (SUPER). A strength of the technique is that the global phase need not be a harmonic function to be removed. If the global phase is a harmonic function satisfying the Laplace equation, it may be removed by existing background phase removal method. The global phase is, however, often not harmonic due to various experimental and physiological causes. For example, eddy current-induced phase may not be harmonic. Bulk susceptibility variation in the lungs during respiration may cause variations in the static magnetic field within the brain tissue (17). The phase shift of the fat signal with respect to water is another source of non-harmonic phase. These non-harmonic phases degrade QSM if they are not properly removed. These phases may have global and non-harmonic characters in common, thus they can be adequately modeled and corrected by SUPER.

The fitting of the global inhomogeneity model causes little error in the tissue susceptibility-induced phase. From the simulation (Fig. 1), the phase error due to the global inhomogeneity fitting appeared small as seen in Figure 1e, and slowly varying. The RMSE in the tissue phase over the entire object was 0.0074 radians. The slowly varying phase would not affect high frequency components of the tissue susceptibility phase, which might be more important in the tissue susceptibility map. The effect of the global fitting on the tissue susceptibility map was also evaluated from the RMSE in the susceptibility map (see the first column in Table 1).

Since the tissue susceptibility-induced phase is locally distributed around the tissue, it would be hardly expressed by the polynomial of degree < 10 over the entire object. A tissue having a relatively large homogeneous volume of susceptibility, such as basal ganglia, may be represented by some lower order polynomial. However, such lower order phase would be largely removed during the QSM processing (background phase removal and deconvolution with the dipole kernel), resulting in little change in the susceptibility map.

Since the global phase modeling by SUPER aims to remove the global inhomogeneity phase while preserving the tissue susceptibility-induced phase, it cannot precisely remove some background susceptibility-induced phase that has local character. For example, the background susceptibility-induced phase at the tissue-air interfaces has high frequency characteristics locally at the boundary, which may not be properly expressed by the polynomial of degree less than 10 (SUPER). It may be better removed by the background phase removal method. Thus, we propose SUPER to be used as a preprocessing method, without replacing existing QSM processing.

Once the global inhomogeneity-induced phase is removed by SUPER, the remaining phase would not have

wrapping problem, since the tissue susceptibility-induced phase is much smaller than π radians in most gradient echo sequences. Thus, the phase unwrapping module in QSM may be bypassed if SUPER is used as a preprocessor. It may be applied repeatedly, however, without trouble, if it is integrated with other processing modules. Phase unwrapping on unwrapped phase would not degrade the data, nor increase RMSE in the susceptibility map as confirmed in the simulation (See RMSE in the parenthesis for the unwrapped phase, which appeared very close to those for the wrapped phase, for both Laplacian unwrapping and SUPER, in Table 1).

The improvements on the small vessel susceptibility mapping, as shown in Figure 5 by correcting slowly varying global inhomogeneity phase, are not fully understood. The improvements may be partially due to the correction of higher order terms of the polynomial, and partially related to the phase unwrapping by removing large global inhomogeneity induced phase by the proposed method. Further investigation is needed. Since the proposed method is based on partial derivatives of the inhomogeneity model, the dc term is not uniquely determined. The dc offset or bias may be removed by calibrating center frequency at shimming. In the experiment, we measured two echoes; however we can extend the proposed method to multiple echo acquisition for multi parametric quantitative imaging. Signal-to-noise would also be improved with multi echo acquisition.

SUPER provides a global inhomogeneity map which is useful not only for removing global inhomogeneity phase but also for separating water and fat signal, which is essential to body QSM (33). Thus, SUPER models the global inhomogeneity phase rather than simply removing it. The estimated global inhomogeneity can also be used to correct voxel shift along the frequency encoding direction (23). Although the voxel misregistration may not be large in conventional brain imaging and gradient-echo based QSM, it could be a serious problem in fast QSM using EPI, where the global inhomogeneity map would be useful to correct geometric distortion as well as the error in the susceptibility map.

In conclusion, the simultaneous phase unwrapping and global field inhomogeneity correction (SUPER) is proposed for QSM. To verify the effectiveness of the method, RMSE in the susceptibility maps are evaluated under various types of global inhomogeneity by numerical simulation. The simulation confirmed that the global inhomogeneity introduces error in the susceptibility map. RMSE in the susceptibility map increased under the influence of global inhomogeneity; while the error was consistent, irrespective of the global inhomogeneity, if the inhomogeneity was corrected by the SUPER technique. Thus, correcting global inhomogeneity before applying QSM is essential to obtain an accurate susceptibility map. The SUPER technique models the inhomogeneity with a polynomial and finds model coefficients using the phase difference data corresponding to the partial derivatives of the model formula, by which phase wrapping and chemical shifts need not be considered.

The technique was applied to *in vivo* QSM imaging with volunteers at 3.0T and 7.0T MRI systems. Some error in small vascular structures in the susceptibility maps under inhomogeneity disappeared if the inhomogeneity was corrected. The global inhomogeneity correction also reduced low frequency fluctuation and non-uniformity in the frontal lobes, where field inhomogeneity was more severe. Since the susceptibility variations are small quantities in the brain tissue, correction of the inhomogeneity is an essential element for obtaining an accurate QSM.

Acknowledgments

This work was supported by the National Research Foundation of Korea (NRF) grant funded by the Korea government (MSIP) (NRF-2015R1A2A2A03005089). The present research has also been conducted by the research grant of Kwangwoon University in 2016.

REFERENCES

1. Salomir R, de Senneville BD, Moonen CT. A fast calculation method for magnetic field inhomogeneity due to an arbitrary distribution of bulk susceptibility. Concepts in Magn Reson Part B (Magn Reson Engineering) 2003;19B: 26-34
2. Cho ZH. Review of recent advancement of ultra high field magnetic resonance imaging: from anatomy to tractography. Investig Magn Reson Imaging 2016;20:141-151
3. Haacke EM, Xu Y, Cheng YC, Reichenbach JR. Susceptibility weighted imaging (SWI). Magn Reson Med 2004;52:612-618
4. Sehgal V, Delproposto Z, Haacke EM, et al. Clinical applications of neuroimaging with susceptibility-weighted imaging. J Magn Reson Imaging 2005;22:439-450
5. Mittal S, Wu Z, Neelavalli J, Haacke EM. Susceptibility-weighted imaging: technical aspects and clinical applications, part 2. AJNR Am J Neuroradiol 2009;30:232-

252

6. Adachi Y, Sato N, Saito Y, et al. Usefulness of SWI for the detection of iron in the motor cortex in amyotrophic lateral sclerosis. J Neuroimaging 2015;25:443-451
7. Santhosh K, Kesavadas C, Thomas B, Gupta AK, Thamburaj K, Kapilamoorthy TR. Susceptibility weighted imaging: a new tool in magnetic resonance imaging of stroke. Clin Radiol 2009;64:74-83
8. Zhang J, Zhang Y, Wang J, et al. Characterizing iron deposition in Parkinson's disease using susceptibility-weighted imaging: an in vivo MR study. Brain Res 2010;1330:124-130
9. Gho SM, Liu C, Li W, et al. Susceptibility map-weighted imaging (SMWI) for neuroimaging. Magn Reson Med 2014;72:337-346
10. de Rochefort L, Liu T, Kressler B, et al. Quantitative susceptibility map reconstruction from MR phase data using bayesian regularization: validation and application to brain imaging. Magn Reson Med 2010;63:194-206
11. Li W, Wu B, Liu C. Quantitative susceptibility mapping of human brain reflects spatial variation in tissue composition. Neuroimage 2011;55:1645-1656
12. Schweser F, Deistung A, Lehr BW, Reichenbach JR. Quantitative imaging of intrinsic magnetic tissue properties using MRI signal phase: an approach to in vivo brain iron metabolism? Neuroimage 2011;54:2789-2807
13. Chen W, Zhu W, Kovanlikaya I, et al. Intracranial calcifications and hemorrhages: characterization with quantitative susceptibility mapping. Radiology 2014;270:496-505
14. Yao B, Li TQ, Gelderen P, Shmueli K, de Zwart JA, Duyn JH. Susceptibility contrast in high field MRI of human brain as a function of tissue iron content. Neuroimage 2009;44:1259-1266
15. Xu B, Liu T, Spincemaille P, Prince M, Wang Y. Flow compensated quantitative susceptibility mapping for venous oxygenation imaging. Magn Reson Med 2014;72:438-445
16. Romeo F, Hoult DI. Magnet field profiling: analysis and correcting coil design. Magn Reson Med 1984;1:44-65
17. Raj D, Anderson AW, Gore JC. Respiratory effects in human functional magnetic resonance imaging due to bulk susceptibility changes. Phys Med Biol 2001;46:3331-3340
18. Van de Moortele PF, Pfeuffer J, Glover GH, Ugurbil K, Hu X. Respiration-induced B0 fluctuations and their spatial distribution in the human brain at 7 Tesla. Magn Reson Med 2002;47:888-895
19. Liu T, Khalidov I, de Rochefort L, et al. A novel background field removal method for MRI using projection onto dipole fields (PDF). NMR Biomed 2011;24:1129-1136
20. Zhou D, Liu T, Spincemaille P, Wang Y. Background field removal by solving the Laplacian boundary value problem. NMR Biomed 2014;27:312-319
21. Langkammer C, Schweser F, Krebs N, et al. Quantitative susceptibility mapping (QSM) as a means to measure brain iron? A post mortem validation study. Neuroimage 2012;62:1593-1599
22. Ahn CB, Jo JM, Cho ZH. Magnetic field homogeneity correction algorithm using pseudoinversion formula for NMR imaging. Rev Sci Instrum 1986;57:683-688
23. Jezzard P, Balaban RS. Correction for geometric distortion in echo planar images from B0 field variations. Magn Reson Med 1995;34:65-73
24. Yang YJ, Park J, Yoon JH, Ahn CB. Field inhomogeneity correction using partial differential phases in magnetic resonance imaging. Phys Med Biol 2015;60:4075-4088
25. Haacke EM, Liu S, Buch S, Zheng W, Wu D, Ye Y. Quantitative susceptibility mapping: current status and future directions. Magn Reson Imaging 2015;33:1-25
26. Schofield MA, Zhu Y. Fast phase unwrapping algorithm for interferometric applications. Opt Lett 2003;28:1194-1196
27. Cusack R, Papadakis N. New robust 3-D phase unwrapping algorithms: application to magnetic field mapping and undistorting echoplanar images. Neuroimage 2002;16:754-764
28. Feng W, Neelavalli J, Haacke EM. Catalytic multiecho phase unwrapping scheme (CAMPUS) in multiecho gradient echo imaging: removing phase wraps on a voxel-by-voxel basis. Magn Reson Med 2013;70:117-126
29. Wang Y, Liu T. Quantitative susceptibility mapping (QSM): decoding MRI data for a tissue magnetic biomarker. Magn Reson Med 2015;73:82-101
30. Bilgic B, Chatnuntawech I, Langkammer C, Setsompop K. Sparse methods for quantitative susceptibility mapping; Wavelets and Sparsity XVI, SPIE, San Diego, USA, 2015;9597:959711-959711-1
31. Kressler B, de Rochefort L, Liu T, Spincemaille P, Jiang Q, Wang Y. Nonlinear regularization for per voxel estimation of magnetic susceptibility distributions from MRI field maps. IEEE Trans Med Imaging 2010;29:273-281
32. Bilgic B, Fan AP, Polimeni JR, et al. Fast quantitative susceptibility mapping with L1-regularization and automatic parameter selection. Magn Reson Med 2014;72:1444-1459
33. Dong J, Liu T, Chen F, et al. Simultaneous phase unwrapping and removal of chemical shift (SPURS) using graph cuts: application in quantitative susceptibility mapping. IEEE Trans Med Imaging 2015;34:531-540